Flow characteristics and intrinsic workability of IN718 superalloy

Fei Chen [a], Juan Liu [b,*], Hengan Ou [a,*], Bin Lu [b,c], Zhenshan Cui [b], Hui Long [c]

[a] Department of Mechanical, Materials and Manufacturing Engineering, The University of Nottingham, Nottingham NG7 2RD, UK
[b] National Die & Mold CAD Eng. Research Center, Shanghai Jiao Tong University, Shanghai, China
[c] Department of Mechanical Engineering, University of Sheffield, Sheffield S1 3JD, UK

A B S T R A C T

This study focuses on deformation characteristics of superalloy IN718 by formulation of a new flow stress model and detailed evaluation of intrinsic workability through the generation of three-dimensional (3D) processing maps with the support of optical microstructural observations. Based on thermomechanical simulation tests using a Gleeble-1500 machine, the flow stress model for superalloy IN718 was built and the flow stress throughout the entire deformation process was described by a peak stress only depending on Zener–Hollomon parameter and strain. The developed model exhibited the strain softening due to dynamic recrystallisation (DRX). The intrinsic workability was further investigated by constructing 3D processing maps. The 3D processing maps described the variations of the efficiency of power dissipation and flow instability domains as a function of strain rate, temperature and strain, from which the favourite deformation conditions for thermomechanical processing of IN718 can be established.

© 2015 The Authors. Published by Elsevier B.V. This is an open access article under the CC BY license (http://creativecommons.org/licenses/by/4.0/).

1. Introduction

In addition to achieving the alteration of their shapes, thermomechanical processing including hot forging is also commonly used to tailor the service properties of metals and alloys through microstructural evolution in industrial production [1]. During hot deformation, material responses can be mainly classified into two categories: dynamic recovery (DRV) and dynamic recrystallisation (DRX). For metals with DRV, the flow stress at a constant strain rate initially increases with the increase of the strain because work hardening is a dominant mechanism in microstructural evolution, and this follows by a steady trend because of the balance between work hardening and DRV. For metals with DRX, the flow stress increases because of work hardening and attains a maximum value, and then the stress decreases because DRX occurs, eventually attaining steady state due to the balance between work hardening and DRX. IN718 superalloy is of typical DRX characteristics under hot deformation conditions [2].

During hot forming processes, such as hot forging and rolling, accurate constitutive equations are crucial for precise measurement and description of local and instantaneous response of the material to the set of thermal and mechanical events in the deformation cycle in numerical simulations [3,4]. Therefore, considerable investigations have been attempted to develop constitutive equations of metals and alloys from experimentally measured data to describe the hot deformation behaviour [5–11]. The critical review paper by Lin et al. [5] provided a summary of the constitutive models that may be divided into three categories: (1) phenomenological constitutive model [6,7], (2) physical-based constitutive model [8,9] and (3) artificial neural network (ANN) flow stress model [10,11]. Each type has its own distinct advantages and disadvantages [5]. Therefore, in order to model the flow stress describing DRX properties for metals and alloys, on one hand, it is highly desirable to develop more laconic and effective model to account for all of the complex dynamic mechanisms. On the other hand, it is essential for the key parameters of the model to be readily obtained through physical simulation experiments, such as hot compression, tension and torsion tests.

In recent years, the processing map has been widely used to identify the deformation temperature and strain rate windows for hot working and to further optimise the hot working process of metals and alloys [12–15]. Frost and Ashby [16], first of all, proposed deformation mechanism map based on creep mechanisms applicable to lower strain rates. Raj [17] extended the concept of Ashby's map to construct processing maps using an atomistic method. Because Raj's processing maps are merely suitable to pure metal and dilute alloys and many fundamental material parameters are required to be determined in advance, for most commercial alloys it is difficult to plot these processing maps proposed by Raj. Based on dynamic material model (DMM) Prasad [18] proposed another approach of processing maps for hard-to-

* Corresponding authors.
E-mail addresses: liujuan@sjtu.edu.cn (J. Liu), H.Ou@nottingham.ac.uk (H. Ou).

deform materials such as titanium alloys, alloy steels and magnesium alloys. This approach has been widely adopted to analyse the intrinsic workability of metals. Prasad's processing maps are a superimposition of a power dissipation map and an instability map under conditions of various temperatures and strain rates. They not only describe the microstructural evolution mechanism and the flow instability regions under certain deformation conditions, but also provide an optimum temperature and strain rate range. However, the conventional two-dimensional (2D) processing maps built by Prasad do not include the variation of strain. So for metals characterized by strain softening, they cannot show the effect of strain on workability. Recently, Liu et al. [14,19] put forward and built 3D processing maps considering strain for a magnesium alloy for the first time, which demonstrated the influence of strain on workability. The 3D processing maps consist of two parts: a 3D power dissipation map and a 3D instability map, describing the distribution of the efficiency of power dissipation and flow instability regions under conditions of various temperatures, strain rates and strains. Therefore, 3D processing map based on the DMM approach provides an effective way to optimise the processing parameters for metals and alloys.

Due to its excellent mechanical characteristics at elevated temperatures up to 650 °C, good fatigue and corrosion resistance, IN718 superalloy has been widely used in aerospace industry [20]. Usually, IN718 superalloy components are made through the close-die forging. The mechanical properties of forgings are extremely sensitive to the thermodynamic variables, such as temperature, strain and strain rate [21]. Therefore, in order to achieve the desired properties of IN718 superalloy forgings, it is important to investigate the hot deformation behaviours and to optimise the thermomechanical processing parameters. On the other hand, in order to accurately simulate hot forging process by means of numerical techniques such as finite element method, it is important to precisely understand the constitutive equations which describe the dependence of the flow stress on the strain, strain rate and temperature. In the past two decades, many studies have been carried out to characterize the high temperature flow behaviour in IN718 [22–32].

In these studies, instead of establishing physically based constitutive equations, phenomenological models have been widely adopted. Zhou and Baker [22] studied the effect of strain rate and temperature on the deformation behaviour for IN718 and proposed a mathematical model to predict the peak stress. Srinivasan et al. [23] developed a constitutive equation in the form of a third-order polynomial function of strain rate independent of strain to describe the flow behaviour of IN718 over the temperature range from 871 °C to 1149 °C and strain rate ranging from 0.001 s^{-1} to 10 s^{-1}. Zhang et al. [24] employed a power-law equation to represent the relationship between flow stress and strain rate at temperature ranging from 960 °C to 1040 °C and at strain rate ranging from 0.001 s^{-1} to 1 s^{-1}. Thomas et al. [25] developed a hyperbolic sine type equation to describe the hot flow behaviour at temperature ranging from 900 °C to 1050 °C and strain rate ranging from 0.005 s^{-1} to 0.1 s^{-1}. Similarly, Wang et al. [26] employed a hyperbolic sine type equation to describe the relationship between peak stress and deformation temperature and strain rate. Similarly, Nowotnik et al. [27,28] studied the dynamic precipitation at elevated temperature. In this work, it was found that the shear banding, cavities growth and intergranular cracks penetrating through the whole grains were the main factors for the decrease in the flow stress at relatively low temperature range. At the same time, a hyperbolic sine Arrhenius type equation was employed to describe the relationship between flow stress and deformation temperature and strain rate. Furthermore, Zhao et al. [29] proposed a dislocation density based state variable to describe the characteristic flow behaviour during hot deformation in

IN718. The hardness-based flow stress model was introduced for IN718 [30]. The effect of the initial workpiece hardness was incorporated into the reference J–C equation. Recently, Jafarian et al. [31] gave a detail investigation on different types of J–C material models for IN718 and found out the most suitable J–C constitutive equation to simulate microstructural and microhardness changes. Lin et al. [32] established a phenomenological constitutive model to describe the coupled effects of deformation temperature, strain rate and strain on the high temperature deformation behaviours of Ni-based superalloy (GH4169).

On the other hand, some investigations on the hot deformation behaviours of IN718 superalloy have been carried out from the point view of microstructural evolution in recent years [33–43]. Zhou and Baker [33] studied the microstructural evolution behaviour during dynamic and metadynamic recrystallisation processes by using hot compression tests. They found that the recrystallised grain size is sensitive to the deformation temperature and strain rate. Medeiros et al. [34] studied the grain size evolution behaviour during dynamic recrystallisation for IN718 superalloy. And the relationship between grain size and thermochemical parameters, such as temperature and strain rate was established. In order to predict the grain size of IN718 superalloy during holding period after hot forging, Zhang et al. [35] investigated the effects of the hot deformation parameters (temperature, strain rate and strain) and holding time on the grain growth by using a mathematical equation. Wang et al. [36] studied the microstructural evolution during dynamic recrystallisation of hot deformed IN718 superalloy and the effects of δ phase on dynamic recrystallisation behaviours. Kuo et al. [37] studied the aging effects of the δ phase on failure, and established the relationship between the microstructure and creep behaviour of IN718 superalloy. Zhang et al. [38] studied the tensile deformation and fracture characteristics of IN718 alloy with different initial δ phase content and found that the elongation of the specimen increases with the increase of the initial δ phase contents and the δ phase and carbide are the nucleuses for the formation of micropores which result in the tensile fracture. Lin et al. [39,40] studied the effects of initial δ phase on the hot tensile deformation behaviours and fracture characteristics of Ni-based superalloy (GH4169). They found that δ phase and carbides are the nucleus for the formation of microvoids, and the δ phase plays a key role in the coalescence of microvoids. Additionally, coupling with the two dimensional processing map, the high temperature deformation behaviours of Ni-based superalloys were also studied by Cai et al. [41], Sui et al. [42] and Wen et al. [43].

The flow behaviour of IN718 superalloy under hot deformation conditions have been extensively researched in recent decades. Due to the significant effects of dynamic recrystallisation on the hot deformation behaviour, as well as the microstructures and mechanical properties of IN718 structural parts, it is desirable to accurately estimate the flow stress during the hot deformation. Furthermore, there is also a clear need for better understanding of the intrinsic workability of IN718 superalloy under hot deformation conditions by coupling with 3D processing maps compared using the traditional 2D processing maps. In this paper, firstly, a new flow stress model for IN718 superalloy under hot deformation was built with the consideration of both macroscopic behaviour and microscopic mechanisms, characterizing the sensitivity of the flow stress to dynamic recrystallisation. Secondly, based on the general approach of processing maps, 3D processing maps with consideration of strain were built, which demonstrated the variation of power dissipation efficiency and flow instability domains at different temperatures, strain rates and strains. As a result, the workability for IN718 superalloy was further evaluated with the support of optical microstructural observations in deformed IN718.

2. Material and experiments

The chemical composition (wt%) of IN718 superalloy used in this study is as follows: 18.07Cr–17.74Fe–5.41Nb–2.86Mo–1.02Ti–0.9Si–0.5Al–0.025C–(bal.)Ni. The diameter and length of the specimens are 8 mm and 12 mm, respectively. The isothermal compression tests were carried out at the temperatures 940 °C, 980 °C, 1020 °C and 1060 °C and at the strain rates 0.001 s^{-1}, 0.01 s^{-1}, 0.1 s^{-1} and 1 s^{-1}. The tests were performed on a Gleeble-1500 thermomechanical simulator. The maximum true strain is 1.0. In order to minimise the frictions during hot deformation, the tantalum foil with the thickness of 0.1 mm was used between the specimen and dies. The stress–strain data were automatically recorded by the testing system during the hot compression. The true stress–true strain curves obtained from the Gleeble tests are shown in Fig. 1. In order to study the effects of the forming processing on the microstructure, the specimens were immediately quenched by water after hot compression. The deformed specimens were sliced along the compression axis section for microstructural analysis. The tested specimens were prepared for optical microscopy (OM) using standard metallographic techniques of mounting, coarse and fine grinding, final polishing and etching. The specimens were immersion etched with HCL (20 ml)+40%HF (50 ml)+H$_2$O$_2$ (2 ml) to reveal the microstructure. Etching times varied with test conditions from 2 to 3 min at room temperature.

3. Modelling of flow stress and determination of parameters

Theoretically, in the flow rule the atomic diffusibility and the driving force of dislocation migration depends on the temperature. The dislocation density and the accumulation of grain boundary energy depend on the strain rate. The flow stress reaches a peak value when the flow driving force and resistance force bring into equilibrium, so the peak stress is a function of temperature and strain rate.

Hot deformation and creep at elevated temperatures have the similar physical mechanism, i.e., thermal activation mechanism. So, the steady flow stress during hot compression tests can be modelled using creep equation, written as the function of the temperature and strain rate. The form is as follows:

$$Z = \dot{\varepsilon} \exp (Q/RT) = f(\sigma) \tag{1}$$

where Z is the temperature-compensated strain rate, i.e. the Zener–Hollomon parameter, $\dot{\varepsilon}$ is strain rate, Q is the effective activation energy for deformation, R is the gas constant, T is temperature, σ is the steady stress.

McQueen and Ryan [44] pointed out that for metals with DRX, σ can be referred to the peak stress σ_p or the start of steady state stress σ_m. The only difference is that the value of Q in terms of σ_p is higher than the value of Q in terms of σ_m. As the value of the peak stress σ_p is easier to be obtained from the Gleeble tests than σ_m, the peak stress σ_p is used in the present study.

Generally, the right side of Eq. (1) is in the form of power function or exponential function or Sellars' hyperbolic sine function [45], as listed below

$$f(\sigma) = A_1 \sigma^{n_1} \tag{2}$$

$$f(\sigma) = A_2 \exp (\beta\sigma) \tag{3}$$

$$f(\sigma) = A_3 (\sinh (\alpha\sigma))^{n_2} \tag{4}$$

where A_1, A_2, A_3, n_1, n_2, α, β are material constants.

The values of A_1 and n_1 can be obtained from the plot of $\ln Z$ versus $\ln \sigma$. The values of A_2 and β can be obtained from the plot of $\ln Z$ versus σ. Sellars [45] pointed that the favourite function is Eq. (2) at the higher stress level and Eq.(3) at the lower stress. So, he proposed the hyperbolic sine model Eq. (4). The values of A_3 and n_2
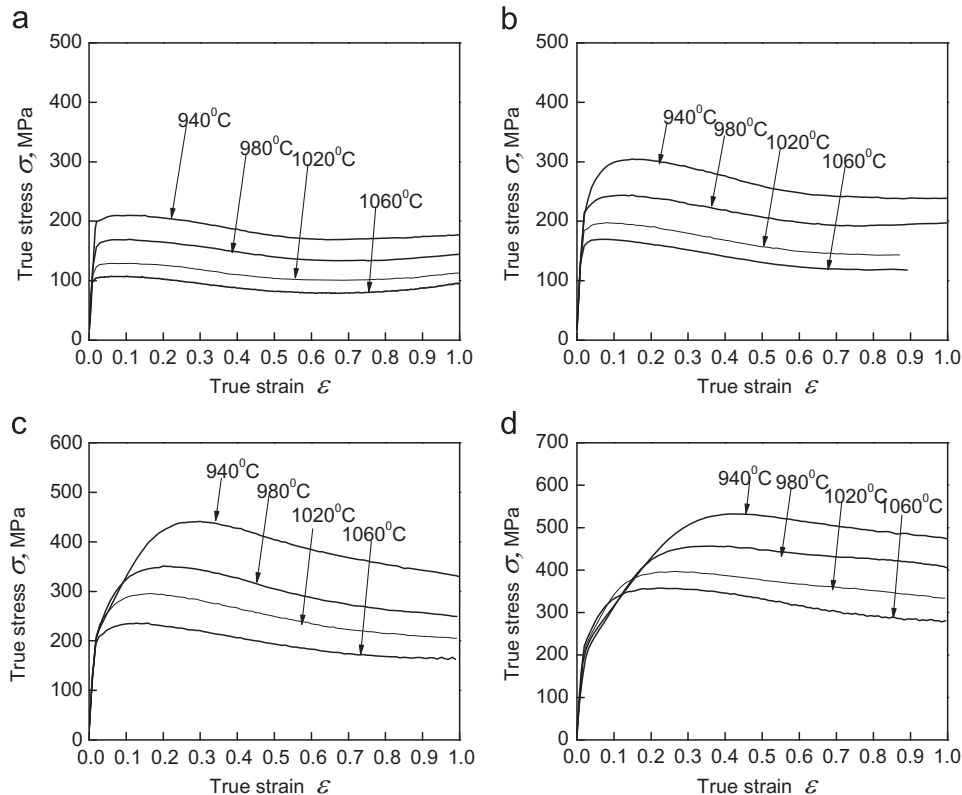

Fig. 1. The true stress–true strain curves of IN718 at various strain rates: (a) $\dot{\varepsilon}=0.001$ s^{-1}, (b) $\dot{\varepsilon}=0.01$ s^{-1}, (c) $\dot{\varepsilon}=0.1$ s^{-1}, (d) $\dot{\varepsilon}=1$ s^{-1}.
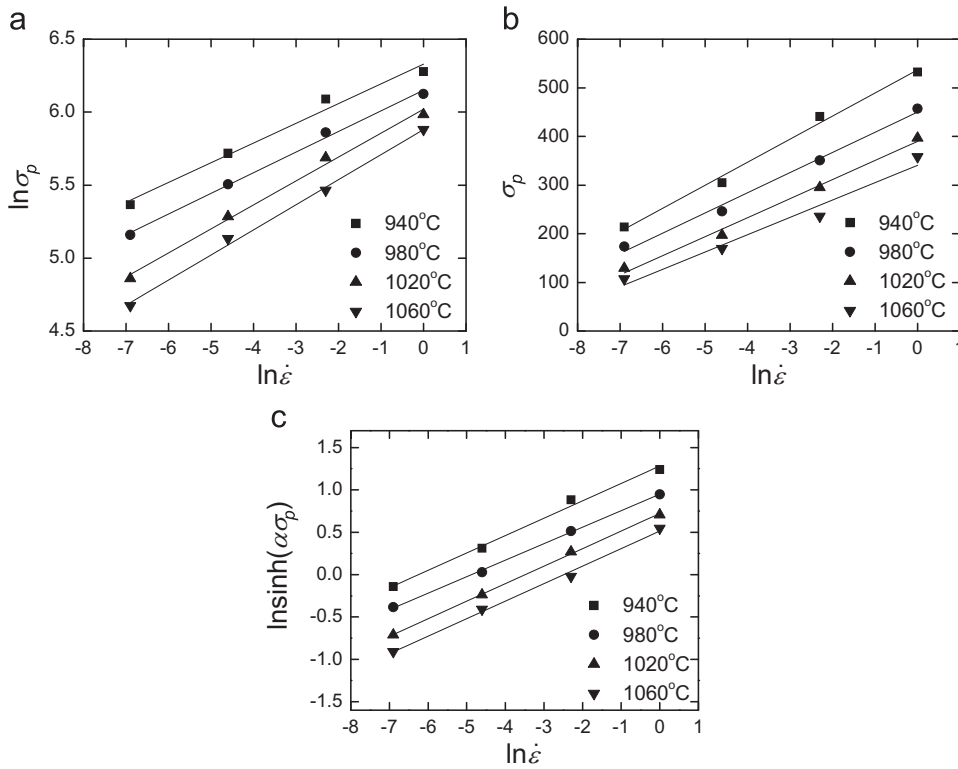
Fig. 2. Schematic of the dependence of the peak stress on strain rate at different temperatures: (a) Schematic of ln σ_p versus ln $\dot{\varepsilon}$, (b) Schematic of σ_p versus ln $\dot{\varepsilon}$ (c) Schematic of ln(sinh($\alpha\sigma_p$)) versus ln $\dot{\varepsilon}$.

can be obtained from the plot of ln Z versus ln(sinh($\alpha\sigma$)). But the values of α must be determined in advance. Assuming the value of n_1 equals n_2, the approximate value of n_2 can be taken as the slope of the plot of ln $\dot{\varepsilon}$ versus ln σ. It can be seen by comparing Eq. (3) with Eq. (4) that A_2 is equal to $A_3/2^n$ and the value of α is approximately equal to β/n_2. The value of A_2 and β can be determined according to the ln $\dot{\varepsilon}$ versus σ plot.

Among Eqs. (2)–(4), Eq. (4) is most widely used, but it has more parameters than Eqs. (2) and (3). In order to choose a reasonable form among Eqs. (2)–(4), the relationship between ln σ_p and ln $\dot{\varepsilon}$ and the relationship between σ_p and ln $\dot{\varepsilon}$ are investigated first, as shown in Fig. 2(a) and (b), from which α can be obtained, 0.0037. Then, the relationship between schematic of ln(sinh($\alpha\sigma_p$)) and ln $\dot{\varepsilon}$ is analysed, as shown in Fig. 2(c). The values of n_1, β and n_2 are 6.6050, 0.0247 and 4.9267, respectively.

The results show that there is excellent linear correlations between ln(sinh($\alpha\sigma_p$)) and ln $\dot{\varepsilon}$ and poor linear correlations between ln σ_p and ln $\dot{\varepsilon}$ and between σ_p and ln $\dot{\varepsilon}$. So Eq. (4) is chosen as the favourite equation to calculate σ_p instead of Eqs. (2) and (3).

From Eq. (4), the value of Q is calculated from the following equation:

$$Q = R \left[\frac{\partial(\ln(\sinh(\alpha\sigma)))}{\partial(1/T)} \right]_{\dot{\varepsilon}} \cdot \left[\frac{\partial \ln \dot{\varepsilon}}{\partial(\ln(\sinh(\alpha\sigma)))} \right]_T \tag{5}$$

on the right-hand side of the above formula the first term represents the slope of the ln(sinh($\alpha\sigma_p$)) versus 1/T plot and the second term represents the reciprocal value of inclination of the ln(sinh($\alpha\sigma_p$)) versus ln $\dot{\varepsilon}$ plot.

By plotting the relation between of σ_p and 1/T as shown in Fig. 3, the mean slope of σ_p versus 1/T is obtained, which is 1.0487×10^4. So the value of Q equals 429.56 kJ/mol.

By Eq. (4),

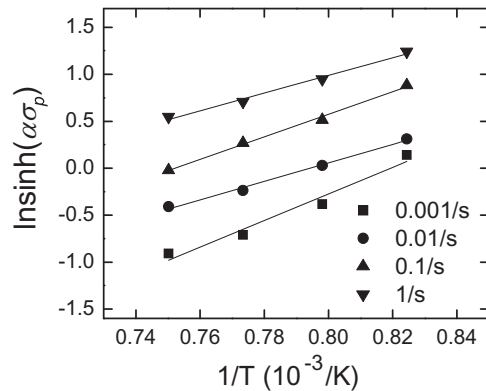$$\ln Z = \ln A + n \ln \left(\sinh(\alpha\sigma_p) \right) \tag{6}$$

Fig. 3. Schematic of ln(sinh($\alpha\sigma_p$)) versus 1/T.

Fig. 4. Schematic of σ_p versus ln Z.

According to Eq. (6), the exact values of A_2 and β are obtained from the σ_p-ln Z plot, as shown in Fig. 4.
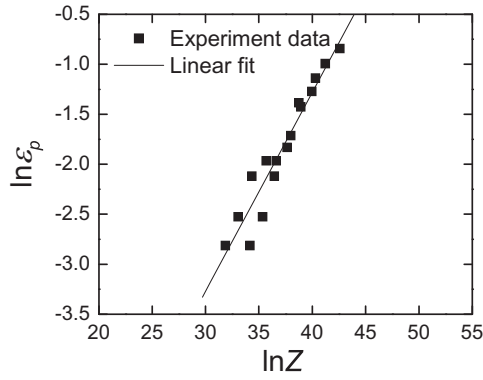
Fig. 5. Schematic of ε_p versus $\ln Z$.

The relationship of σ_p and Z is expressed as follows:

$$\sigma_p = \frac{1}{\alpha} \cdot \ln \left(\left(\frac{Z}{A} \right)^{1/n} + \left(\left(\frac{Z}{A} \right)^{\frac{2}{n}} + 1 \right)^{1/2} \right) \tag{7}$$

where α is 0.0037, n is 4.9058, A is 6.2625×10^{15}.

Considering the work softening due to DRX in the hot working process, the peak strain was used to build the flow stress model. The relationship of ε_p and the Z parameter is obtained according to Fig. 5 and the simplified form is as follow:

$$\ln \varepsilon_p = B_1 \ln Z + B_2 \tag{8}$$

where B_1 is 0.1989, B_2 is -9.2385.

Based on the equation describing the dependence of the peak stress on the temperature and strain rate in the previous section, the formula expressing the dependence of the flow stress at different strain on the strain and the peak stress will be built in this section. Liu et al. [6] analysed the relationship of the difference of the flow stress at different strain and the peak stress with the increasing strain and proposed a new model to reflect the work softening due to DRX. The form is as follows:

$$\frac{\ln \sigma - \ln \sigma_p}{\ln \xi \varepsilon} = \eta \left(\frac{\varepsilon - \varepsilon_p}{\varepsilon_p} \right)^2 \tag{9}$$

Eq. (9) can also be written as

$$\ln \sigma = \psi (\varepsilon - \varepsilon_p)^2 \ln \xi \varepsilon + \ln \sigma_p \tag{10}$$

where ψ and ξ are material constants.

The hot deformation process is a complex process in which work hardening and DRX coexist and interact. During the DRX process, work hardening does not cease entirely. In fact, it is difficult to determine the dynamic recrystallised volume fraction by means of measuring method in quantitative metallography since it is hard to distinguish between recrystallised microstructure and work-hardened microstructure. In Eq. (9), the left side is referred to 'strain softening exponent', and the right side is the function of the peak strain. Eq. (9) not only represents the softening process due to DRX but also has some advantages in contrast with the classic formula of the dynamic recrystallised volume fraction. In classic equations, the critical strain is considered as the peak strain multiplied by a factor between 0.60 and 0.85. This factor is not determined easily. This model bypasses the calculation of ε_c, which improves the model's precision.

It can be found that according to Eq. (10) the new model contains only two parameters: ξ and Ψ. In fact, Eq. (10) can be calculated from two pairs of experimental values. For multiple experimental values, the optimum value of ξ and Ψ can be obtained by the least-squares method. The value of ξ equals 0.6993; the value of Ψ equals to 1.2.

According to Eq. (9), the flow stress curve graphs can be
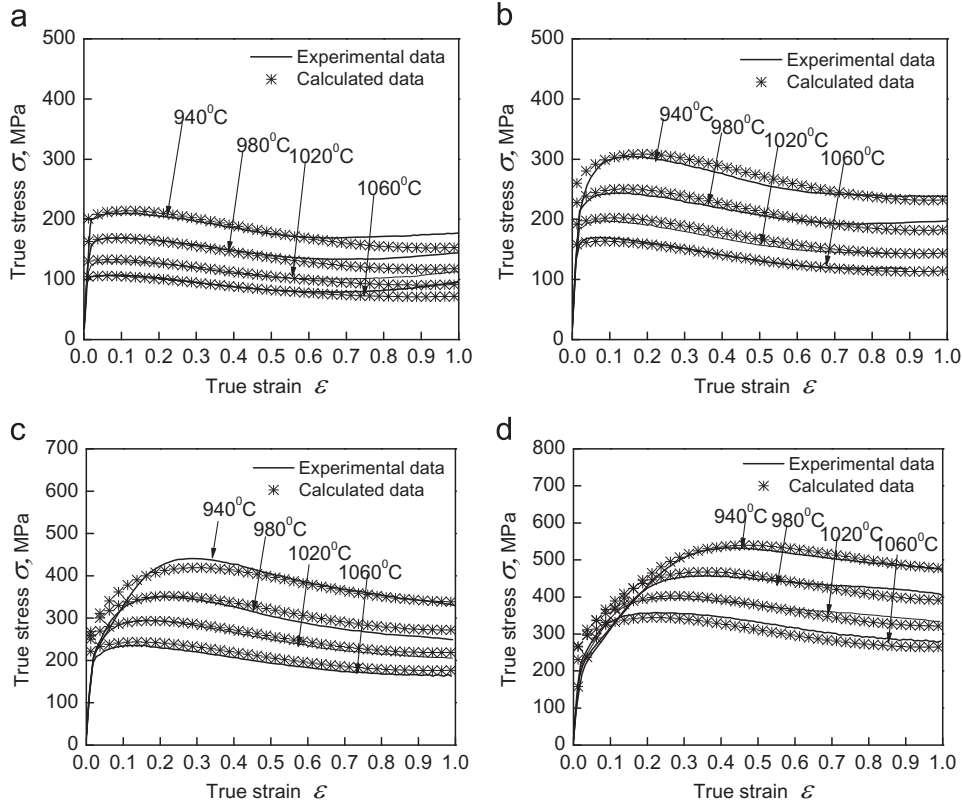

Fig. 6. Comparison between model prediction results and experimental results of IN718: (a) $\dot{\varepsilon} = 0.001 \text{ s}^{-1}$, (b) $\dot{\varepsilon} = 0.01 \text{ s}^{-1}$, (c) $\dot{\varepsilon} = 0.1 \text{ s}^{-1}$, (d) $\dot{\varepsilon} = 1 \text{ s}^{-1}$.
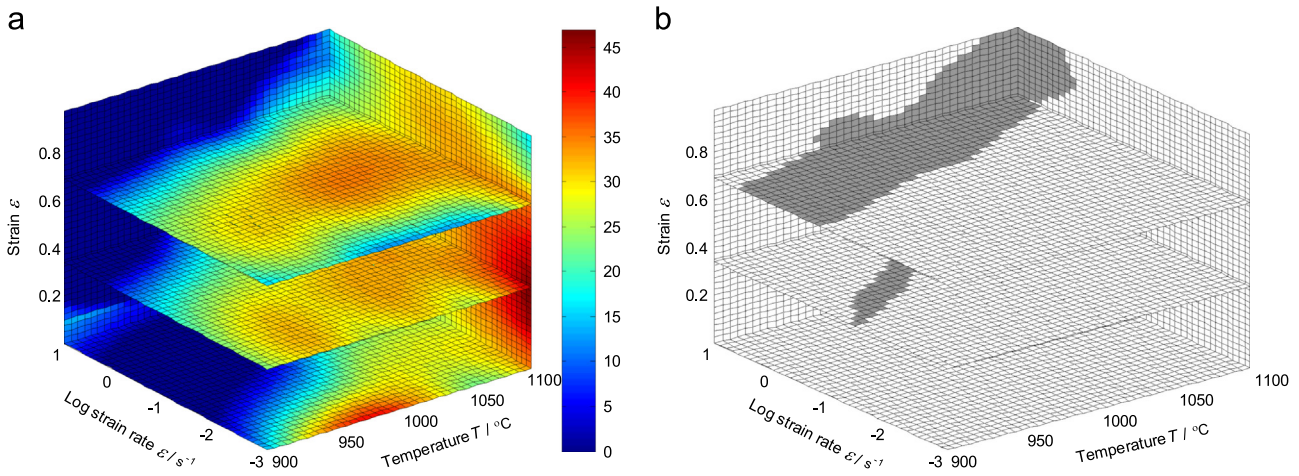
Fig. 7. (a) The 3D power dissipation maps and (b) the 3D flow instability map at strain 0.4 and 0.7.
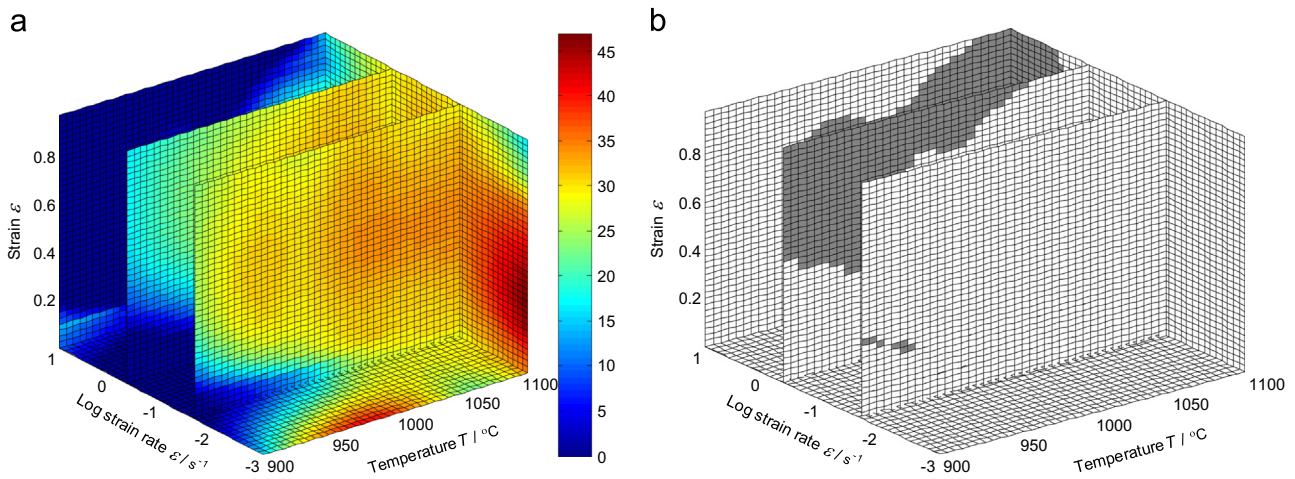

Fig. 8. (a) The 3D power dissipation maps and (b) the 3D flow instability map at strain rate 0.01, 1 and 10 s^{-1}.
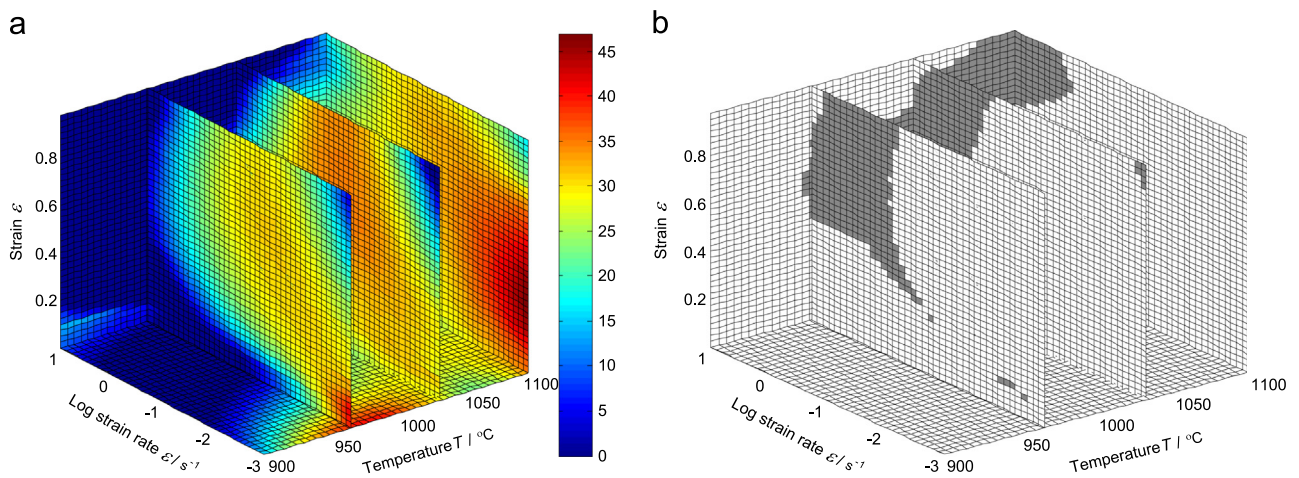

Fig. 9. (a) The 3D power dissipation maps and (b) the 3D flow instability map at temperature 980, 1020 and 1100 °C.

sketched as Fig. 6. Obviously, the flow stress curves modelled by Eq. (9) demonstrated a good correlation with the results obtained from experiments. In conclusion, according to this new model the expression is given for the flow stress at different strains, temperatures and strain rates. Furthermore, the new flow stress model includes fewer parameters, which are easier to be determined. Therefore, the new model is suitable for implementation into commercial software for numerical simulation of hot forging

process for IN718 superalloy.

4. Intrinsic workability analysis

Processing maps are based on dynamic material model, which was firstly developed by Prasad [18]. The flow stress, when strain and deformation temperature are constants, is given by
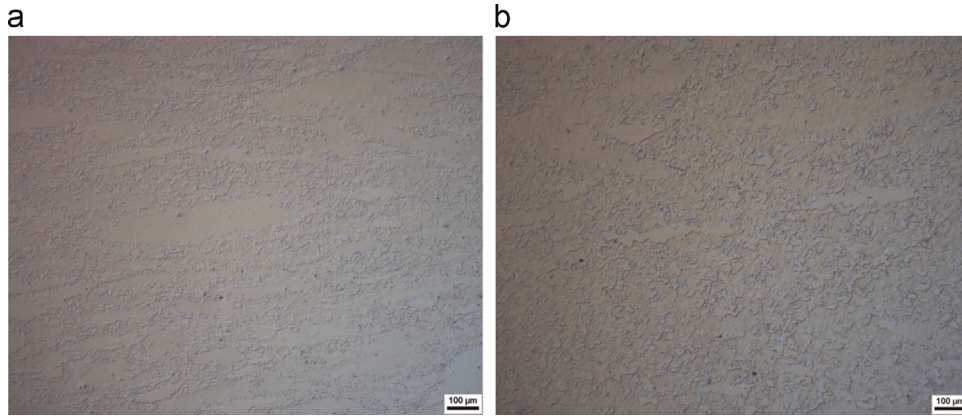
Fig. 10. Optical microstructure of superalloy IN718 at strain rate of 0.001 s^{-1} and temperatures: (a) 980 °C and (b) 1020 °C.
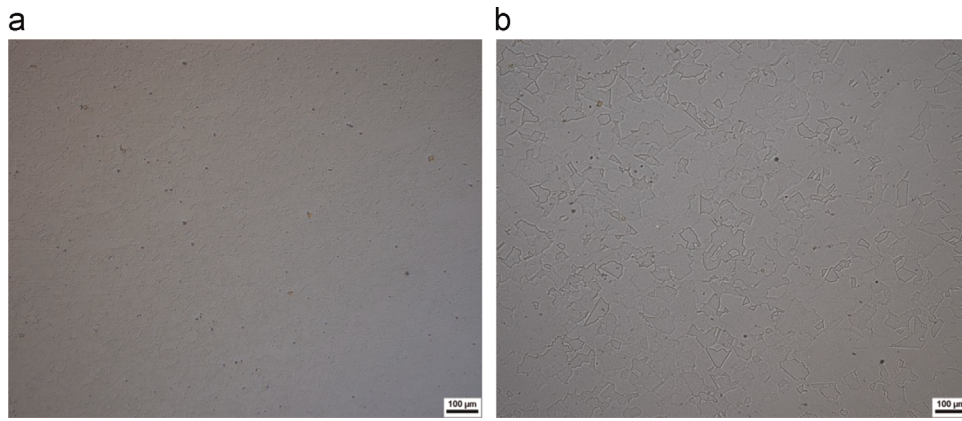

Fig. 11. Optical microstructure of superalloy IN718 at 1100 °C and strain rate: (a) 0.01 s^{-1} and (b) 0.001 s^{-1}.
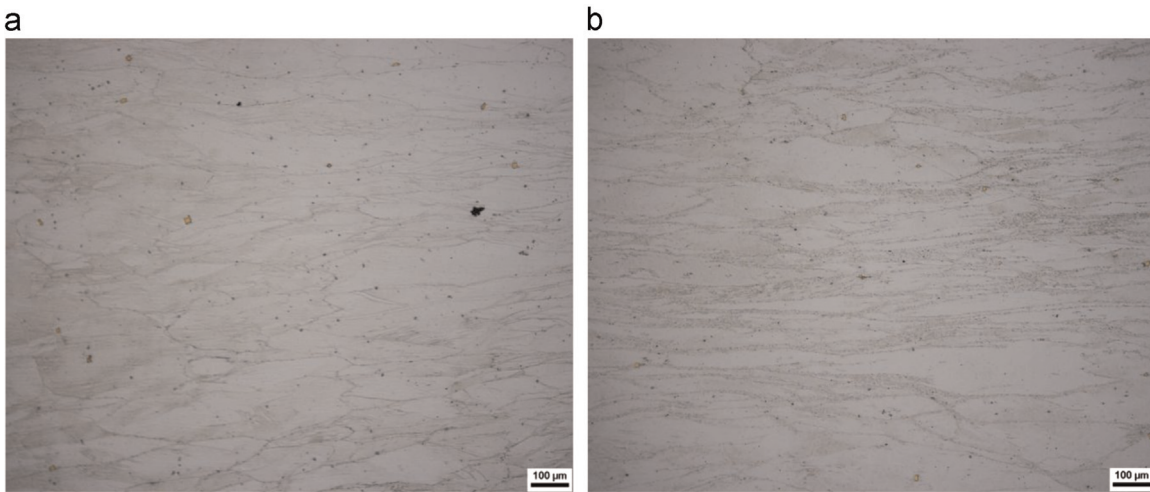

Fig. 12. Optical microstructure of superalloy IN718 at strain rate of 1 s^{-1} and temperature: (a) 980 °C and (b) 1060 °C.

$$\sigma = K\dot{\varepsilon}^m \tag{11}$$

where K is a material constant, m is strain rate sensitivity

$$m = \partial(\ln \sigma)/\partial(\ln \dot{\varepsilon}) \tag{12}$$

The workpiece undergoing hot deformation can be considered as a dissipator of power. The total power P may be separated into two complementary functions

$$P = \sigma\dot{\varepsilon} = G + J = \int_0^{\dot{\varepsilon}} \sigma d\dot{\varepsilon} + \int_0^{\sigma} \dot{\varepsilon} d\sigma \tag{13}$$

where G content represents the power dissipation due to plastic deformation, and J co-content represents the power dissipation due to metallurgical changes.

$$\frac{dJ}{dG} = \frac{\dot{\varepsilon} d\sigma}{\sigma d\dot{\varepsilon}} = \frac{d \ln \sigma}{d \ln \dot{\varepsilon}} = \left|\frac{\partial(\ln \sigma)}{\partial(\ln \dot{\varepsilon})}\right|_{\varepsilon,T} = m \tag{14}$$

By comparison of J co-content with the maximum possible dissipation J_{max}, the efficiency of power dissipation—a dimensionless parameter η is given by

$$\eta = J/J_{max} = 2m/(m + 1) \tag{15}$$

Instability maps are developed on the basis of an instability criterion proposed by Ziegler [46]. Instable flow occurs if the differential quotient satisfies the inequality

$$\frac{dJ}{d\dot{\varepsilon}} < \frac{J}{\dot{\varepsilon}} \tag{16}$$

By a dimensionless parameter, instability is given by

$$\xi(\dot{\varepsilon}) = \frac{\partial \ln (m/(m + 1))}{\partial \ln \dot{\varepsilon}} + m < 0 \tag{17}$$

The 3D maps of power dissipation and flow instability at different strains, strain rates and temperatures are shown in Figs 7–9. In the power dissipation maps the colour of grid denotes the value of efficiency of power dissipation (shown as a percentage) and in the flow instability maps the grey domains correspond to flow instability of material.

According to the 3D processing maps, it is proved that the efficiency of power dissipation and the flow instability domain vary considerably with increasing strain. When the strain is less than 0.6, it shows that the efficiency of power dissipation increases with the increase of strain, and then the efficiency of power dissipation decreases with the increase of strain from 0.6 to 0.8 at higher temperature and lower strain rates. The efficiency of power dissipation increases with the increase of the temperature from 900 °C to 1000 °C at lower strain rate and slightly decreases with the increase of temperature from 1000 °C to 1100 °C. The efficiency of power dissipation increases with the increase of the temperature at lower strain rate. The efficiency of power dissipation decreases with the increase of the strain rate at lower temperatures and increases with the increase of strain rate at higher temperatures. The flow instability domains are located at higher strain rates and increases with the increase of strain. The 3D processing maps exhibit two maximum power dissipation efficiency domain and one flow instability domain.

(1) The first domain of maximum efficiency of power dissipation occurs at 980–1020 °C and 0.001 s^{-1} with a peak efficiency of 35–40%. The second domain of maximum efficiency of power dissipation occurs at 1100 °C and 0.001–0.01 s^{-1} with a peak efficiency of 45%. Some research came to the conclusion that the dominant deformation mechanism in this region is due to dynamic recrystallisation [47]. The efficiency of power dissipation increased with the increase of strain. Considering that the higher deformation velocity is available, these two domains are considered as the most favourite region for hot deformation. The microstructures of superalloy IN718 in the first deformation region are shown in Fig. 10. The grains are finer at temperature 980 °C and grow with increasing temperature. Meanwhile, the dynamic recrystallised fraction increases with increase of temperature. In other words, the higher the forming temperature, the greater the degree of dynamic recrystallisation. However, as shown in the figure it can be easily found that the complete dynamic recrystallisation does not occur under these two deformation conditions. Fig. 11 shows the optical microstructure at 1100 °C and strain rate of 0.01 s^{-1} and 0.001 s^{-1}. It can be seen that this allows full recrystallisation to occur. With the increase of strain rate, it can make the grain finer when strain rate is higher under the same deformation temperature. The main mechanism is summarized below. There are increased dislocation generation rate, the dislocation density and nucleation sites in the deformed microstructure area. For the case of high strain rate, there are more deformation energies stored in the deformed superalloy IN718. Therefore, it is generally accepted that more substructures can be generated in the initial grain boundary when strain rate is higher, which produces more nuclei per unit volume of the grains.

(2) Regarding the instability regions shown in Figs 7–9. It can be found that the flow instability occurs at 1–10 s^{-1} and 900–1060 °C. The typical microstructure behaviours in flow instability zones include the occurrence of adiabatic shear bands and flow localisation [48]. The microstructures of the specimens deformed at 980 °C/1 s^{-1} and 1060 °C/1 s^{-1} are shown in Fig. 12 (a) and (b), respectively. It shows that the elongated grains with serrations developed in the grain boundaries can be observed. It is easily found that the material undergoes flow localisation. When the material was formed at high strain rates, the small recrystallised grains were formed at the original grain boundary which provides a path where slip can occur easily. Deformation was concentrated in this area and then flow localisation bands were produced [14]. Flow localisation is undesirable for obtaining consistent mechanical properties. Therefore, the hot deformation process should not be performed in these regions.

5. Conclusions

The flow behaviours and workability of the IN718 superalloy were investigated under different forming temperatures and strain rates. A new flow stress model was developed and the processing maps were constructed. Two specific conclusions to be drawn from this study.

(1) As a function of the peak stress and strain, a new flow stress equation was developed to characterize dynamic recrystallisation of IN718 under hot deformation conditions. This new model gives a good description of the flow behaviour during DRX. As compared to traditional flow stress models, only two material parameters are needed to derive the flow stress model, which can be beneficial for identification of the parameters and its practical application.
(2) With the consideration of strain, a new set of 3-D processing maps were developed, which provided a quantitative assessment of the distributions of the efficiency of power dissipation and flow instability domains of IN718 under different strain rate, temperature and strain conditions. The 3D processing maps show two maximum power dissipation efficiency domains as a favourable deformation condition, whilst, on the other hand, the identified flow instability domain should be avoided. This is of a particular advantage in providing guidelines for actual hot deformation operation of IN718 superalloys.

References

[1] Y.S. Na, J.T. Yeom, N.K. Park, J.Y. Lee, Simulation of microstructures for alloy 718 blade forging using 3D FEM simulator, J. Mater. Process. Technol. 141 (2003)

337–342.

[2] Y.C. Lin, D.X. Wen, J. Deng, G. Liu, J. Chen, Constitutive models for high-temperature flow behaivors of a Ni-based superalloy, Mater. Des. 59 (2014) 115–123.

[3] F. Chen, Z.S. Cui, J. Chen, Prediction of microstructural evolution during hot forging, Manuf. Rev. 1 (6) (2014) 1–21, http://dx.doi.org/10.1051/mfreview/2014006.

[4] F. Chen, F.C. Ren, Z.S. Cui, X.M. Lai, Constitutive modeling for elevated temperature flow behavior of 30Cr2Ni4MoV ultra-super-critical rotor steel, J. Iron Steel Res. Int. 21 (2014) 521–526.

[5] Y.C. Lin, X.M. Chen, A critical review of experimental results and constitutive descriptions for metals and alloys in hot working, Mater. Des. 32 (2011) 1733–1759.

[6] J. Liu, Z.S. Cui, C.X. Li, Modelling of flow stress characterizing dynamic recrystallization for magnesium alloy AZ31B, Comput. Mater. Sci. 41 (2008) 375–382.

[7] Y.C. Lin, M.S. Chen, J. Zhong, Constitutive modeling for elevated temperature flow behavior of 42CrMo steel, Comput. Mater. Sci. 42 (2008) 470–477.

[8] J. Qu, Q.L. Jin, B.Y. Xu, Parameter identification for improved viscoplastic model considering dynamic recrystallization, Int. J. Plast. 21 (2005) 1267–1302.

[9] X.G. Fan, H. Yang, Internal-state-variable based self-consistent constitutive modeling for hot working of two-phase titanium alloys coupling microstructure evolution, Int. J. Plast. 27 (2011) 1833–1852.

[10] Y.C. Lin, J. Zhang, J. Zhong, Application of neural networks to predict the elevated temperature flow behavior of a low alloy steel, Comput. Mater. Sci. 43 (2008) 752–758.

[11] V. Valaichelvi, D. Sivakumar, R. Karthikeyan, K. Palanikumar, Prediction of the flow stress of 6061 Al-15% SiC-MMC composites using adaptive network based fuzzy inference system, Mater. Des. 30 (2009) 1362–1370.

[12] N. Srinivasan, Prasad YVRK, P. Rama Rao, Hot deformation behaviour of Mg–3Al alloy – a study using processing map, Mater. Sci. Eng. A 476 (2008) 146–156.

[13] Y.C. Lin, L.T. Li, Y.C. Xia, Y.Q. Jiang, Hot deformation and processing map of a typical Al–Zn–Mg–Cu alloy, J. Alloy. Compd. 550 (2013) 438–445.

[14] J.Q. Li, J. Liu, Z.S. Cui, Characterization of hot deformation behavior of extruded ZK60 magnesium alloy using 3D processing maps, Mater. Des. 56 (2014) 889–897.

[15] Z.N. Yang, F.C. Zhang, C.L. Zheng, M. Zhang, B. Lv, L. Qu, Study on hot deformation behaviour and processing maps of low carbon bainitic steel, Mater. Des. 66 (2015) 258–266.

[16] H.J. Frost, M.F. Ashby, Deformation Mechanism Maps, Pergamon Press, Oxford, 1982.

[17] R. Raj, Development of a processing map for use in warm-forming and hot forming processes, Metall. Trans. A 12 (1989) 1089–1097.

[18] Gegel H.L. Prasad YVRK, S.M. Doraivelu, J.C. Malas, J.T. Morgan, K.A. Lark, D.R. Barker, Modeling of dynamic material behavior in hot deformation: forging of Ti-6242, Metall. Trans. A 15 (1984) 1883–1892.

[19] J. Liu, Z.S. Cui, C.X. Li, Analysis of metal workability by integration of FEM and 3-D processing maps, J. Mater. Process. Technol. 205 (2008) 497–505.

[20] D.H. Kim, J.H. Kim, J.W. Sa, Y.S. Lee, C.K. Park, S.I. Moon, Stress rupture characteristics of Inconel 718 alloy for ramjet combustor, Mater. Sci. Eng. A 483–484 (2008) 262–265.

[21] Y.C. Lin, M.S. Chen, J. Zhong, Effects of deformation temperature on stress/strain distribution and microstructural evolution of deformed 42CrMo steel, Mater. Des. 30 (2009) 908–913.

[22] L.X. Zhou, T.N. Baker, Effect of strain rate and temperature on IN718 during high temperature deformation, Mater. Sci. Eng. A 177 (1994) 1–9.

[23] R. Srinivasan, V. Ramnarayan, U. Deshpande, V. Jain, I. Weiss, Computer simulation of the forging of fine grain IN-718 alloy, Metall. Trans. A 24 (1993) 2061–2069.

[24] J.M. Zhang, Z.Y. Gao, J.Y. Zhuang, Z.Y. Zhong, Mathematical modelling of the hot-deformation behavior of superalloy IN718, Metall. Mater. Trans. A 30 (1999) 2701–2712.

[25] A. Thomas, M. EL-Wahabi, J.M. Cabrera, J.M. Prado, High temperature deformation of Inconel 718, J. Mater. Process. Technol. 177 (2006) 469–472.

[26] Y. Wang, W.Z. Shao, L. Zhen, X.M. Zhang, Microstructure evolution during dynamic recrystallization of hot deformed superalloy 718, Mater. Sci. Eng. A 486 (2008) 321–332.

[27] A. Nowotnik, P. Pędrak, J. Sieniawski, M. Góral, Mechanical properties of hot deformed Inconel 718 and X750, J. Achiev. Mater. Manuf. Eng. 46 (2008) 74–80.

[28] A. Nowotnik, Effect of high temperature deformation on the structure of Ni based superalloy, J. Achiev. Mater. Manuf. Eng. 50 (2012) 115–122.

[29] X. Zhao, R.P. Guest, S. Tin, D. Cole, J.W. Brooks, M. Peers, Modelling hot deformation of Inconel 718 using state variables, Mater. Sci. Technol. 20 (2004) 1414–1420.

[30] A.D. Prete, L. Filice, D. Umbrello, Numerical simulation of machining nickel-based alloys, Procedia CIRP 8 (2013) 539–544.

[31] F. Jafarian, M. Imaz Ciaran, D. Umbrello, P.J. Arrazola, L. Filice, H.F. Amirabadi, Element simulation of machining Inconel 718 alloy including microstructure changes, Int. J. Mech. Sci. 88 (2014) 110–121.

[32] Y.C. Lin, X.M. Chen, D.X. Wen, M.S. Chen, A physically-based constitutive model for a typical nickel-based superalloy, Comput. Mater. Sci. 83 (2014) 282–289.

[33] L.X. Zhou, T.N. Baker, Effects of dynamic and metadynamic recrystallization on microstructures of wrought IN-718 due to hot deformation, Mater. Sci. Eng. A 196 (1995) 89–95.

[34] S.C. Medeiros, Prasad YVRK, W.G. Frazier, R. Srinivasan, Modeling grain size during hot deformation of IN718, Scr. Mater. 40 (2000) 17–23.

[35] M.J. Zhang, Z.Y. Gao, J.Y. Zhuang, Z.Y. Zhong, Grain growth model of IN718 during holding period after hot deformation, J. Mater. Process. Technol. 101 (2000) 25–30.

[36] Y. Wang, W.Z. Shao, L. Zhen, B.Y. Zhang, Hot deformation behaviour of delta-processed superalloy 718, Mater. Sci. Eng. A 528 (2011) 3218–3227.

[37] C.M. Kuo, Y.T. Yang, H.Y. Bor, C.N. Wei, C.C. Tai, Aging effects on the microstructure and creep behavior of Inconel 718 superalloy, Mater. Sci. Eng. A 510–511 (2009) 289–294.

[38] S.H. Zhang, H.Y. Zhang, M. Cheng, Tensile deformation and fracture characteristics of delta-processed Inconel 718 alloy at elevated temperature, Mater. Sci. Eng. A 528 (2011) 6253–6258.

[39] Y.C. Lin, J. Deng, Y.Q. Jiang, D.X. Wen, G. Liu, Hot tensile deformation behaviors and fracture characteristics of a typical Ni-based superalloy, Mater. Des. 55 (2014) 949–957.

[40] Y.C. Lin, J. Deng, Y.Q. Jiang, D.X. Wen, G. Liu, Effects of initial d phase on hot tensile deformation behaviors and fracture characteristics of a typical Ni-based superalloy, Mater. Sci. Eng. A 598 (2014) 251–262.

[41] D.Y. Cai, L.Y. Xiong, W.C. Liu, G.D. Sun, Y. Mei, Characterization of hot deformation behavior of a Ni-based superalloy using processing map, Mater. Des. 30 (2009) 921–925.

[42] F.L. Sui, L.X. Xu, L.Q. Chen, X.H. Liu, Processing map for hot working of Inconel 718 alloy, J. Mater. Process. Technol. 211 (2011) 433–440.

[43] D.X. Wen, Y.C. Lin, H.B. Li, X.M. Chen, J. Deng, L.T. Li, Hot deformation behavior and processing map of a typical Ni-based superalloy, Mater. Sci. Eng. A 591 (2014) 183–192.

[44] H.J. McQueen, N.D. Ryan, Constitutive analysis in hot working, Mat. Sci. Eng. A 322 (2002) 43–63.

[45] C.M. Sellars, Modelling microstructural development during hot rolling, Mater. Sci. Technol. 6 (1990) 1072–1081.

[46] H. Ziegler, An Introduction to Thermomechanics, North-Holland publishing company, Amsterdam New York Oxford, 1983.

[47] G.W. Liu, Y. Han, Z.Q. Shi, J.P. Sun, D.N. Zou, G.J. Qiao, Hot deformation and optimization of process parameters of an as-cast 6Mo superaustenitic stainless steel: a study with processing map, Mater. Des. 54 (2014) 662–672.

[48] Y. Liu, R. Hu, J.S. Li, H.C. Kou, H.W. Li, H. Chang, H.Z. Fu, Characterization of hot deformation behaviour of Haynes230 by using processing maps, J. Mater. Process. Technol. 209 (2009) 4020–4026.